Review of
Scientific Instruments

RESEARCH ARTICLE | FEBRUARY 02 2026

# Multi-filter diamond array time-of-flight particle detector in laser–plasma experiments

Angelo M. Raso ✉ ; Edoardo Domenicone; Giada Petringa ; Fabrizio Consoli ; Farmesk Abubaker ; Massimiliano Scisciò; G. A. Pablo Cirrone ; Shubham Agarwal ; Massimo Alonzo ; Carmen Altana ; Sahar Arjmand ; Caterina Ciampi; Mattia Cipriani ; Pooja Devi ; Francesco Filippi ; Pavel Gajdos ; Benoist Grau; Giovanni Luca Guardo ; Josef Krasa ; Michal Krupka ; Salvatore Mirabella ; Giovanni Morello ; Massimo Nocente ; Fabrizio Odorici ; Gabriele Pasquali ; Antonino Picciotto ; Rosaria Rinaldi; Marcin Rosinski ; Antonino Scandurra ; Sushil Singh ; Przemyslaw Tchorz ; Gianluca Verona Rinati ; Claudio Verona

Check for updates

*Rev. Sci. Instrum.* 97, 023301 (2026)
https://doi.org/10.1063/5.0302424

View Online Export Citation

## Articles You May Be Interested In

Laser-initiated $p$–$^{11}$B fusion reactions in petawatt high-repetition-rate laser facilities

*Matter Radiat. Extremes* (April 2025)

Radioisotope production using lasers: From basic science to applications

*Matter Radiat. Extremes* (March 2024)

Experimental and computational evaluation of alpha particle production from laser-driven proton–boron nuclear reaction in hole-boring scheme

*Phys. Plasmas* (January 2025)

AIP Publishing

Review of
Scientific Instruments

ARTICLE

pubs.aip.org/aip/rsi

# Multi-filter diamond array time-of-flight particle detector in laser–plasma experiments

**Cite as: Rev. Sci. Instrum. 97, 023301 (2026); doi: 10.1063/5.0302424**
**Submitted: 15 September 2025 • Accepted: 23 December 2025 •**
**Published Online: 2 February 2026**

View Online Export Citation CrossMark

**Angelo M. Raso,**[1,2,a)] **Edoardo Domenicone,**[3,4,5] **Giada Petringa,**[6] **Fabrizio Consoli,**[2,3] **Farmesk Abubaker,**[6,7] **Massimiliano Scisciò,**[2,3] **G. A. Pablo Cirrone,**[6,8] **Shubham Agarwal,**[9,10] **Massimo Alonzo,**[2,3] **Carmen Altana,**[6] **Sahar Arjmand,**[6] **Caterina Ciampi,**[11,12,13] **Mattia Cipriani,**[2,3] **Pooja Devi,**[9,10] **Francesco Filippi,**[3,14] **Pavel Gajdos,**[15] **Benoist Grau,**[1,3] **Giovanni Luca Guardo,**[6] **Josef Krasa,**[9] **Michal Krupka,**[9,15] **Salvatore Mirabella,**[16,17] **Giovanni Morello,**[18,19,20] **Massimo Nocente,**[4,5] **Fabrizio Odorici,**[21] **Gabriele Pasquali,**[12,13] **Antonino Picciotto,**[22] **Rosaria Rinaldi,**[18,23] **Marcin Rosinski,**[24] **Antonino Scandurra,**[16] **Sushil Singh,**[9,15,25] **Przemyslaw Tchorz,**[24] **Gianluca Verona Rinati,**[1] **and Claudio Verona**[1,2]

## AFFILIATIONS

[1] Department of Industrial Engineering, University of Rome "Tor Vergata," Via del Politecnico 1, 00133 Rome, Italy
[2] Istituto Nazionale di Fisica Nucleare, Sez. di Roma Tor Vergata, Via della Ricerca Scientifica, Roma, Italy
[3] ENEA CR Frascati, Nuclear Department, Via Enrico Fermi 45, 00044 Frascati, Italy
[4] Department of Physics, University of Milano-Bicocca, 20126 Milan, Italy
[5] INFN, Sez. di Milano Bicocca, Milano, Italy
[6] Laboratori Nazionali del Sud, INFN, Via S. Sofia 62, Catania 95125, Italy
[7] College of Science, Charmo University, Chamchamal, 46023 Sulaymaniyah, Iraq
[8] Centro Siciliano di Fisica Nucleare e Struttura della Materia, Via S. Sofia 62, Catania, Italy
[9] FZU - Institute of Physics, Czech Academy of Sciences, Na Slovance 1999/2, 182 00 Prague, Czech Republic
[10] Faculty of Mathematics and Physics, Charles University, 121 16 Prague, Czech Republic
[11] Grand Accélérateur National d'Ions Lourds (GANIL), CEA/DRF–CNRS/IN2P3, Boulevard Henri Becquerel, F-14076 Caen, France
[12] INFN - Section of Milan, Milan, Italy
[13] Department of Physics and Astronomy, University of Florence, 50019 Sesto Fiorentino, Italy
[14] Istituto Nazionale di Fisica Nucleare - Laboratori Nazionali di Frascati LNF, 00044 Frascati, RM, Italy
[15] Institute of Plasma Physics, Czech Academy of Sciences, Za Slovankou 1782/3, 182 00 Prague, Czech Republic
[16] Department of Physics and Astronomy, University of Catania, Via S. Sofia 64, Catania, Italy
[17] INFN - Section of Catania, Catania, Italy
[18] INFN - Section of Lecce, Lecce, Italy
[19] CNR IMM–Institute for Microelectronics and Microsystems - University of Lecce, Via per Monteroni, 73100 Lecce, Italy
[20] Center for Biomolecular Nanotechnologies, University of Lecce, Istituto Italiano di Tecnologia, Via Barsanti, I–73010 Arnesano, LE, Italy
[21] INFN, Sez. di Bologna, Bologna, Italy
[22] Sensors and Devices Centre - Fondazione Bruno Kessler, Trento, Italy
[23] University of Lecce, Lecce, Italy
[24] Institute of Plasma Physics and Laser Microfusion, 01-497 Warsaw, Poland
[25] Faculty of Electrical Engineering, Czech Technical University in Prague, Prague, Czech Republic

[a)] **Author to whom correspondence should be addressed:** angelomaria.raso@students.uniroma2.eu and angelomariaraso@gmail.com

## ABSTRACT

Recent advances in ion diagnostics for laser-induced plasma experiments have improved system design and data analysis. Measuring charged particle emissions from laser-irradiated targets provides valuable insights into laser–matter interactions. Among real-time diagnostics, Time-of-Flight (TOF) detectors are reliable systems for analyzing particle beam properties such as kinetic energy and shot-to-shot reproducibility. Diamond-based detectors are ideal for TOF measurements due to their fast response time, radiation hardness, and low leakage current. However, TOF detectors lack particle discrimination. To overcome this, a Multi Filter Diamond Array (MFDA) was developed using six nominally identical single crystal diamond detectors paired with aluminum foils of different thicknesses to exploit particle stopping power differences. The MFDA was tested at the Prague Asterix Laser System during an experimental campaign in the framework of the FUSION project, and data analysis was performed. A cross-validation with other diagnostics, including a Thomson Parabola Spectrometer and CR-39 detectors, is also presented.

https://doi.org/10.1063/5.0302424

## I. INTRODUCTION

Recent advances in high-power laser technology have significantly improved the ability to accelerate particles through laser–plasma interactions. These compact systems can generate dense ion bunches with energies reaching hundreds of MeV,[1,2] opening pathways for applications such as radiobiology,[3,4] cultural heritage,[5] and inertial confinement fusion (ICF).[6] In the latter application, among the various fusion reactions under investigation, the deuterium–tritium (DT) reaction remains the most studied, largely due to its high cross section at relatively low temperatures. However, its practical implementation is hindered by significant technical and radiological challenges.[7] As a promising alternative, proton–boron fusion $^{11}\mathrm{B}(p,\alpha)2\alpha$ is attracting growing interest for its aneutronic nature and the production of multiple alpha particles as reaction products.[8–10] Particle generation in laser–plasma environments, such as protons and heavier ions, is highly sensitive to both laser parameters and target configurations.[1,11] For this reason, precise diagnostics of both the incident ions and the resulting fusion products are essential for interpreting experimental outcomes and optimizing future setups. Thomson Parabola Spectrometers (TPSs), nuclear track detectors such as CR-39, and Time-of-Flight (TOF) systems are among the most widely used diagnostics. TOF diagnostics, such as silicon carbide and diamond detectors, provide real-time measurements of ion energy spectra and are indispensable for evaluating shot-to-shot reproducibility and beam characteristics.[12–18]

Thanks to its physical properties, single crystal diamond offers excellent performance as a TOF detector due to its high sensitivity, fast temporal response, and strong radiation tolerance.[19,20] Nonetheless, TOF systems cannot inherently discriminate among ion species, since the time-of-flight depends only on velocity. This makes species identification ambiguous when signals from different particles overlap in time. For example, a 1 MeV proton, a 4 MeV alpha, and a 12 MeV $C^{6+}$ ion all share the same velocity and, thus, TOF value, making species identification impossible based only on this measurement. This challenge becomes particularly important in laser–plasma experiments, where multiple ion species, such as protons, alpha particles, carbon, and other ions, can be accelerated simultaneously. Other diagnostics, such as the mentioned CR-39 and TPS, often face limitations in distinguishing between ion species, particularly when signals overlap for ions with the same charge-to-mass ratio (i.e., TPS) or when ions produce similar track features in etched detectors (i.e., CR-39). While some studies have demonstrated the potential for particle species discrimination using CR-39 and TPS detectors,[21–28] such analyses rely on time-consuming post-processing methods. More recently, a prototype array of TOF diamond detectors has been demonstrated for particle discrimination in laser-driven fusion experiments.[29] The present work can be regarded as a continuation of that effort, extending the concept toward a systematic development of a detector for real-time particle species identification, together with a novel methodology to achieve it.

In this work, we present the development and test of a novel TOF diagnostic system, the Multi Filter Diamond Array (MFDA), composed of six synthetic single crystal diamond detectors (each equipped with an aluminum filter of different thickness), designed to improve ion species discrimination in laser–plasma experiments. The MFDA exploits the use of differential energy loss through aluminum filters combined with synthetic signal modeling. In addition to ion analysis, the system also enables a preliminary estimation of x-ray emission characteristics, providing further insight into the plasma environment.[30] The MFDA was preliminary tested at the Prague Asterix Laser System (PALS) facility by confirming observations consistent with those obtained from diagnostics such as the TPS and CR-39. A method for cross-checking between the MFDA signals and these diagnostics is also presented. The experimental results illustrate the potential of this detector to enhance analysis capabilities and contribute to a more comprehensive understanding of laser-driven particle acceleration and fusion experiments.

## II. MATERIALS AND METHODS

### A. Multi-filter diamond array (MFDA) detector

Six synthetic single crystal diamond radiation detectors with a sandwich structure, incorporating a metal/intrinsic diamond/metal configuration, were realized at the University of Rome "Tor Vergata" laboratories. The fabrication included a high-purity intrinsic single crystal diamond layer deposited through Microwave Plasma Enhanced Chemical Vapor Deposition (MPCVD) onto a low-cost substrate of High-Pressure High Temperature (HPHT) diamond,

$4 \times 4 \times 0.5$ mm$^3$ in size. The CVD diamond layer was grown to a sufficient thickness and then underwent precision laser-cutting by Almax easyLab,[31] separating it from the substrate to a total thickness of 35 $\mu$m. Such diamond thickness was chosen to ensure good temporal resolution (and thus energy resolution) and high radiation hardness.[32] Two chromium contacts (80 nm thick and $2.5 \times 2.5$ mm$^2$ cross section) were thermally evaporated on both diamond surfaces, needed for collecting the electron–hole pairs generated inside the sensitive volume of the detector. A printed circuit board (PCB) featuring six integrated bias tee units ($R = 1$ M$\Omega$, $C = 1$ $\mu$F) with common bias was realized [Fig. 1(c)]. Each diamond detector [Fig. 1(a)] was wire-bonded to the bias tee circuit and glued to the PCB ground with silver paint. An aluminum housing was constructed inside a KF-100 vacuum flange [Figs. 1(b) and 1(d)] to shield from electromagnetic pulse (EMP) noise and to host two CR-39 detectors. Six circular pinholes (2.8 mm diameter), each equipped with an aluminum filter of varying thickness, were positioned ~2 cm in front of the corresponding detectors. Assuming a distance of 1 m from a point-like target, each diamond unit subtends a solid angle of $\sim 6 \times 10^{-4}$ sr, defining the angular acceptance for the incoming particles. To ensure that each detector is properly exposed through its corresponding pinhole, without being geometrically shadowed by the housing, a minimum distance of 35 cm between the target and the center of the MFDA front flange is required. Furthermore, the six detectors are positioned on a circumference of 1 cm radius. At a distance of 1 m from the laser–plasma interaction point, this corresponds to an angle of ~0.6° between the central axis and each detector, and ~1.1° between two diametrically opposite detectors.

### B. Data analysis: Synthetic TOF simulation code

To analyze the measured MFDA signals, a synthetic Time-of-Flight simulation code (SToF) was developed in Python using pre-computed SRIM results for particle stopping powers in matter.[33] The code processes input particle energy distribution and retrieves the TOF signal expected from diamond detectors after the particles have traversed a specified thickness of aluminum. In diamond detectors, the relationship between the generated charge $Q$ and the number $N$ of interacting particles of energy $E$ is

$$Q = \frac{e \cdot N \cdot E \cdot CCE(E)}{\varepsilon}, \tag{1}$$

where $e$ is the electron charge, $\varepsilon = 13.2$ eV is the electron–hole pair production energy in diamond, $CCE(E)$ is the charge collection efficiency, and $E$ is the particle kinetic energy, obtained from the time-of-flight value $t$ through the relativistic relation,

$$E = mc^2\left(\frac{1}{\sqrt{1-(L/tc)^2}} - 1\right), \tag{2}$$

where $L$ is the detector–target distance. In the case of partial absorption, $E$ corresponds to the energy lost inside the detector. Assuming that significant variations of the signal do not occur over time scales comparable to the oscilloscope sampling interval, the energy spectrum for a given ion species can then be obtained by time deriving Eq. (1),[34]

$$\frac{dN}{dE} = \frac{\varepsilon}{e}\frac{V(t)}{RE^2}\left(-\frac{1}{2}t - \delta t\right), \tag{3}$$

where $V(t)$ is the signal amplitude, $R$ is the total resistance of the readout circuit (50 $\Omega$), and $\delta t$ is the sampling time (negligible for fast oscilloscopes). Equation (3) shows that it is still possible to invert the relation and determine the amplitude of the signal as a function of the key variables,

$$V \equiv V(dNdE^{-1}, E, t). \tag{4}$$

When foil filters are used, the value of $E$ should be interpreted as the residual energy of the particle after it has passed through the filter. This residual energy can be calculated using SRIM, which provides the stopping power $S(E) = -dE/dx$ of ions in matter. The energy loss through a filter of thickness $z$ is then obtained by integrating $S(E)$,

$$\Delta E = \int_0^z S(E(x))\, dx, \tag{5}$$

where $E(x)$ is the energy of the particle at position $x$ inside the material. Subtracting this value from the initial energy gives the residual energy used as input in the signal reconstruction. The corresponding TOF value $t$ is then obtained by inverting Eq. (2), under the assumption that the filter is placed close to the detector compared to the full path length from the target. This approximation holds as long as the particles considered are well above the filter's stopping threshold.[35] Finally, the value of the simulated signal is scaled with the geometric acceptance of the detector.

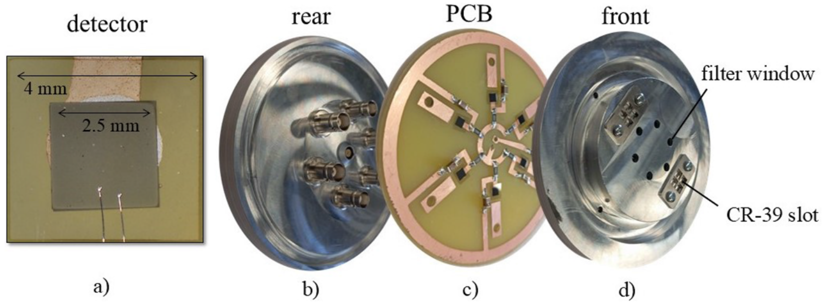

**FIG. 1.** (a) Diamond detector glued to the PCB ground with silver paint and wire-bonded to the bias tee circuit. (b) Rear and (d) front part of the aluminum housing. (c) PCB hosting six diamond detectors and a bias tee circuit.

### C. Particle discrimination methodology

To illustrate the particle discrimination methodology of the MFDA, we consider a beam emitted from a target, composed of two ion species: protons (up to 3 MeV) and fully ionized carbon ions ($C^{6+}$, up to 18 MeV), as reported in Fig. 2(a) (left axis). Neglecting ion–ion collisions, their velocity distribution can be approximated by a Maxwell–Boltzmann (MB) function,[36,37] a common starting point in modeling laser-driven ion emissions, i.e., the Target Normal Sheath Acceleration (TNSA) mechanism. In practice, ion spectra often deviate from a single MB distribution and are better described by a combination of multiple MB or empirical fits.[38] The maximum energy values are arbitrary but correlated by assuming that ions undergo the same sheath acceleration mechanism so that their energy scales as $E = z_i e\phi$, where $\phi$ is the sheath potential and $z_i$ is the charge state of the ion.[1,39] In addition, we consider a distribution of alpha particles centered around 4 MeV [right axis of Fig. 2(a)], adopted as a simplified starting point inspired by the known resonance peak of the proton–boron reaction at 675 keV.[40] However, this approximation does not reflect the actual alpha energy spectrum expected in laser–plasma experiments, where broader distributions are typically observed. It neglects both the low-energy contribution of fusion-produced alphas and the potential momentum transfer from protons to alphas, which could alter the observed

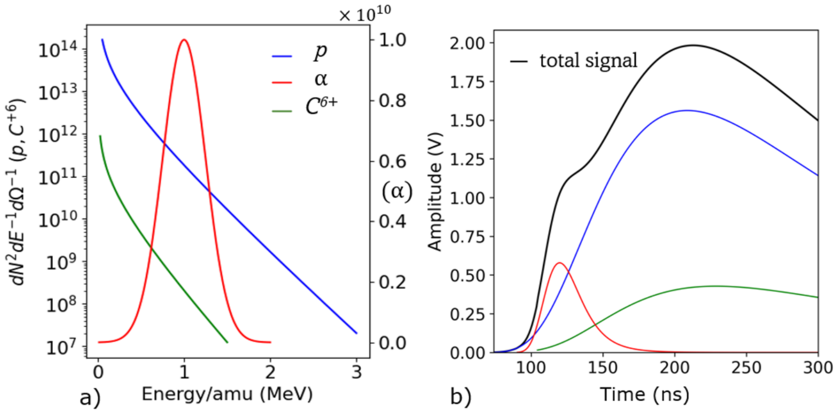

**FIG. 2.** (a) Energy distribution of protons (blue), alphas (red), and fully stripped carbon ions (green). (b) Simulated total TOF signal (black) generated from a three-species system (colored).

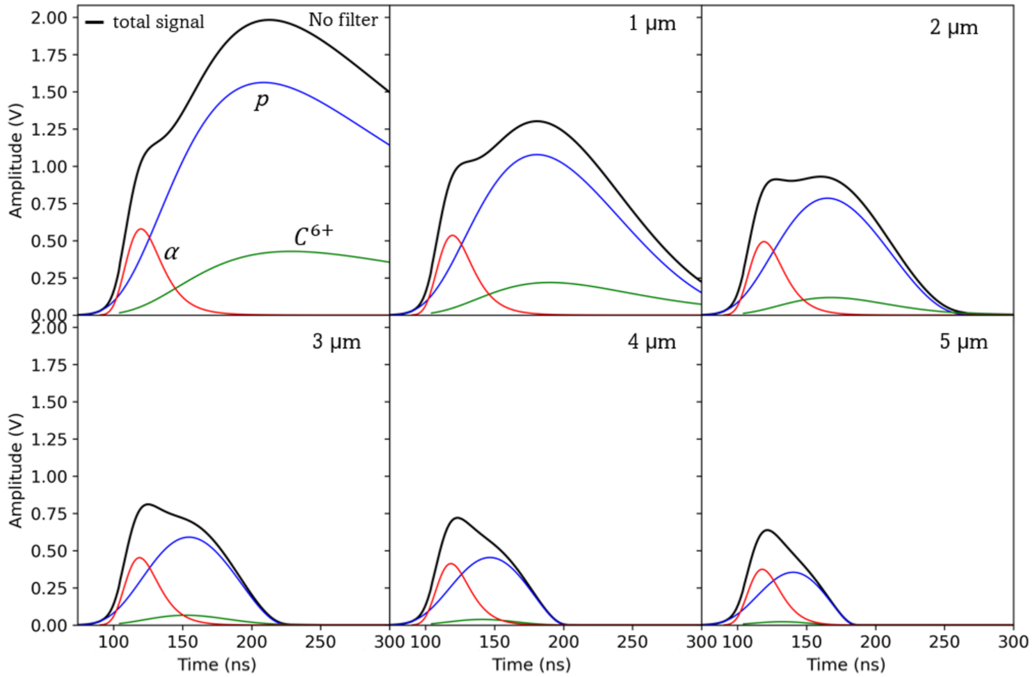

**FIG. 3.** Signal modulations of a three-species system due to increasing aluminum filter thickness.

distribution. The chosen model serves purely as a reference case for illustrative purposes.

Once the geometric parameters, such as distance from the target, detector area, and efficiency, are defined, the total TOF signal can be reconstructed by summing the contributions from the three ion populations. This is shown in Fig. 2(b), where the black line represents the total signal, and the colored lines indicate individual species contributions: blue for protons, green for carbons, and red for alphas. Supposing now a series of detectors equipped with aluminum filters of increasing thickness, one would observe signals whose amplitudes decrease progressively with filter thickness (i.e., 0, 1, 2, 3, 4, 5 $\mu$m), as shown in Fig. 3. The shape of each signal also changes due to the nonlinear dependence of attenuation on both energy and particle type. These findings suggest that it is possible to exploit these distinct signal modulations to achieve partial discrimination between ion species. Indeed, the differing attenuation patterns act as a kind of "spectral fingerprint," allowing individual species to be inferred even when their arrival times overlap. It is important to note that the amplitude of each species' signal depends on the parameters chosen for its distribution, particularly the absolute number of particles and their energy.

## III. RESULTS AND DISCUSSION

### A. MFDA characterization

Each diamond detector unit was first tested in a vacuum using 5.48 MeV alpha particles emitted by a $^{241}$Am source to evaluate its temporal response and charge collection efficiency (CCE). To appreciate the temporal response by single-particle detection, the outputs of the diamond detectors were sent to a fast wideband preamplifier (CAEN A1423B) and then to a fast scope (2 GHz bandwidth, 20 GS/s, Lecroy 620ZI). Each detector unit was set with −90 V bias voltage. As shown in Fig. 4(a), the single alpha pulse was collected with a FWHM of ~1 ns for basically all six detector units. The output signals of the diamonds were also processed by a calibrated conventional charge-sensitive electronic chain consisting of a charge sensitive preamplifier (ORTEC 142A) and a shaping amplifier (ORTEC-570). A multichannel analyzer (ORTEC-927) was then employed to obtain a pulse height spectrum (PHS). Results for all detectors are summarized in Fig. 4(b), and a CCE of ~100% was obtained. Diamond detectors were also characterized at INFN LNL laboratories at Legnaro (Italy) through the Ion Beam Induced Charge (IBIC) technique at the AN2000 micro-beam accelerator using 1 MeV protons as probes to evaluate the homogeneity of the CCE over the whole detector area. In Fig. 4(c), the result of one of the detectors is shown, and the whole contact area responds with uniform efficiency, apart from the two micro-wire-bonding "shadows" clearly visible on the left of the image. It is worth noting that the active area is a key parameter for solid angle computation to correctly reconstruct particle spectra emitted from the target. In Fig. 4(d), the corresponding PHS obtained in parallel is also reported, whose peak at 1 MeV corresponds to the IBIC map acquired.

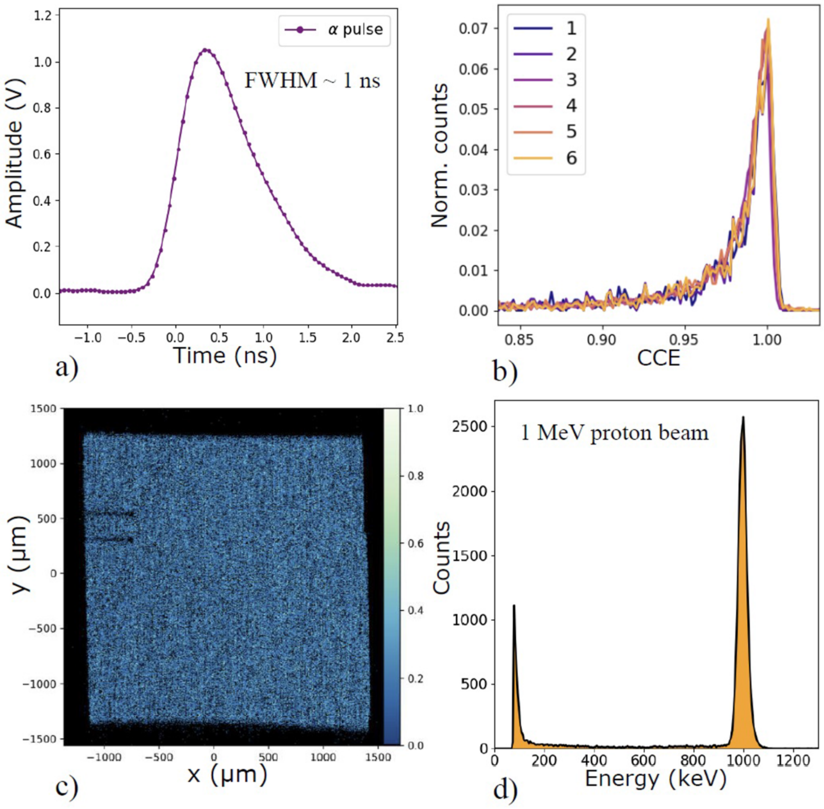

**FIG. 4.** (a) Collected single-$\alpha$ pulse ($^{241}$Am) showing FWHM ~ 1 ns at −90 V bias. (b) PHS from all six MFDA units indicating ~100% CCE. (c) IBIC map (1 MeV protons, AN2000) showing uniform response over the contact area; wire-bonding shadows are visible. (d) PHS from one of the diamonds. The peak at 1 MeV corresponds to the IBIC map acquired.

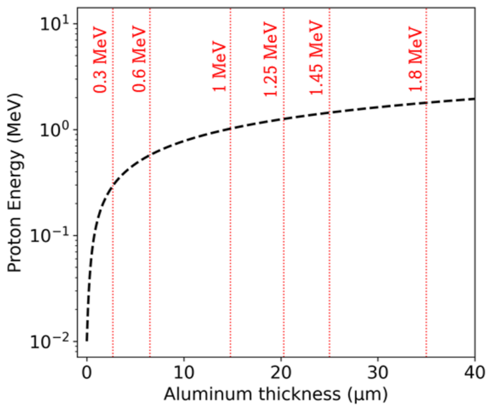

**FIG. 5.** Proton energy thresholds as a function of aluminum foil thickness used in front of the MFDA detectors.

Each thickness of aluminum filters, with nominal values of 3, 6, 15, 20, 25, and 35 $\mu$m, was precisely measured exploiting the stopping power of 5.48 MeV alpha particles. Using the same procedure mentioned before (PHS), we measured the alpha spectrum from each detector with a different thickness of Al filters. The fraction of energy lost for each Al filter was then compared with simulated results using a Monte Carlo simulation Geant4 code[41–43] in order to extrapolate the effective thicknesses of Al filters. The procedure led to accurate values of 2.7, 6.5, 14.8, and 20.3 $\mu$m with an uncertainty of ~3%. The 25 and 35 $\mu$m thick Al filters were not evaluated due to the limited alpha particle range. The corresponding proton threshold energies required to penetrate these filters are reported in Fig. 5.

## B. Experimental setup at the Prague Asterix laser system

The MFDA detector was employed for the study and characterization of laser–plasma experiments during an experimental campaign at the Prague Asterix Laser System (PALS) facility equipped with the iodine laser beam of 600 J energy at the fundamental wavelength (1315 nm) and with 350 ps pulse duration. Various types of solid targets were irradiated with the PALS laser to investigate proton–boron nuclear interactions, with the aim of measuring alpha particle emission from the front side of the target, i.e., the laser-irradiated surface. In Fig. 6, a schematic view of the interaction chamber is shown. The MFDA was mounted 1.27 m far from the target at an angle of 53° from the target normal and at 21° above the equatorial plane. The MFDA was biased with -90 V and connected to fast digital scopes (1 GHz, 10 GS/s) through six double-shielded cables, i.e., RG223. Scopes were mounted inside a Faraday cage equipped with an uninterruptible power supply (UPS) to isolate the front-end acquisition system from the EMP noise generated by the laser–target interaction.[44]

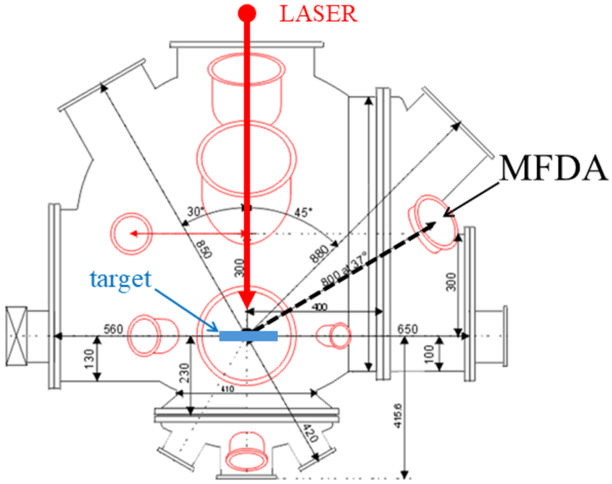

**FIG. 6.** Top view of the PALS interaction chamber featuring the main components. The red line indicates the laser pulse focused on the target. The MFDA is located on a flange at 53° from the primary target normal and 21° above the equatorial plane.

## C. Test at PALS facility

Typical TOF signals acquired by the MFDA are shown in Fig. 7, displaying six individual tracks from a single shot (No. 60 776). The numerical label in the plot increases with the thickness of the filters used. A narrow photopeak, at $t \sim 0$ ns, is clearly visible, and then a broad signal is due to protons and ions of different energies reaching the device. A good signal-to-noise ratio is achieved, with negligible EMP interference. As expected, in the thicker Al filter, a large amount of low-energy particles are stopped (which in the TOF domain corresponds to higher time values), and furthermore, the overall signal becomes increasingly attenuated. Moreover, the temporal cutoff observed in each signal is consistent with the expected proton energy thresholds imposed by the respective aluminum filters. The first detector, equipped with the thinnest filter, appears to be affected by saturation effects due to the very high ion flux impinging on it. In addition, the distinct peaks observed in the signal recorded by the detector with a 6.5 $\mu$m Al filter are attributed to proton energy spectra that significantly deviate from an ideal Boltzmann-like distribution. Such spectral features were independently confirmed by other diagnostics, such as the TPS. From the TPS data (not shown), the $C^{6+}$ ions in this shot reached maximum energies of about 14.5 MeV, which are below the transmission thresholds of most MFDA filters. As a result, only the first two detectors could register a partial contribution from carbon ions, while the others primarily detected protons.

## D. X-ray photopeak attenuation and mean energy estimate

A quick analysis regarding the photopeak intensity due to the x-ray mean energy is feasible through the MFDA. Indeed, the photopeak intensity $Y$ refers to the maximum value of the prompt signal attributed to x-ray emission, as observed in the time-of-flight track. As the thickness of the aluminum filter increases, $Y$ decreases exponentially due to the progressive attenuation of the x-ray signal. This behavior is illustrated in Fig. 8, where the normalized ratio $Y/Y_0$ is plotted as a function of the aluminum filter thickness (for this shot, the 35 $\mu$m filter was replaced with an 18 $\mu$m one). Here,

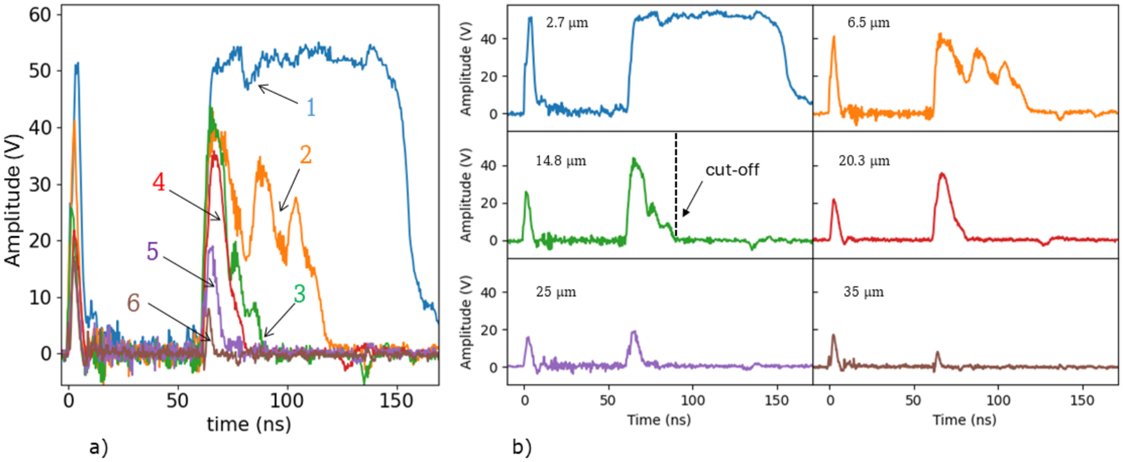

**FIG. 7.** TOF signals from the MFDA for shot No. 60 776: (a) overview (collective view) of the six channels and (b) individual plots for each detector ordered by increasing Al-filter thickness.

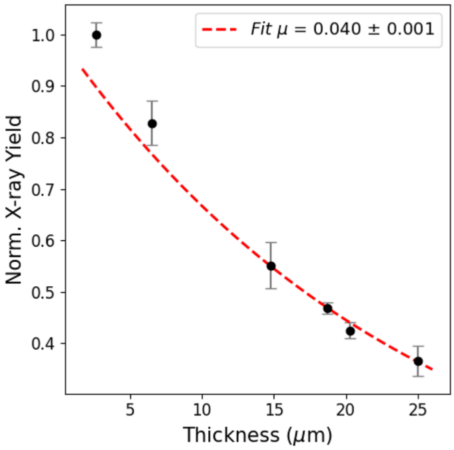

**FIG. 8.** X-ray transmission $Y/Y_0$ vs aluminum thickness $z$ used in the MFDA. The solid line is an exponential fit yielding $\mu \approx 0.04\ \mu\text{m}^{-1}$ (shot No. 60 843).

$Y_0$ represents the photopeak intensity measured with the thinnest filter (2.7 $\mu$m), which is used as a reference for the normalization. Following the methodology reported in Ref. 45, the normalized ratios are fitted using an exponential decay model,

$$Y = Y_0 \exp(-\mu z), \tag{6}$$

where $z$ is the filter thickness and $\mu$ is the attenuation coefficient of x rays in aluminum.

For shot No. 60 843 (laser energy ~480 J), as an example, a $\mu = 0.04\ \mu\text{m}^{-1}$ was obtained. Knowing the aluminum density $\rho$ and the aluminum absorption dependence of the photon energy,[46] an estimated value of ~6 keV was obtained. Such energy is interpreted as the mean value of the emitted x-ray spectrum from the laser–plasma interaction. While this approach does not reconstruct the full spectral distribution, it provides a rough estimate that can serve as a benchmark for future comparisons or alternative diagnostic methods. However, the detector spectral response can influence the result by biasing the measurement toward the most efficiently detected photon energies. Despite these limitations, the technique offers a fast and practical means for preliminary characterization of effective x-ray emission.

## E. Comparison with Thomson parabola spectrometer

For each TOF signal, it is possible to extract the proton spectrum, following the method described previously [Eq. (3)]. Indeed, for most of the experiments of laser–matter interaction, for the maximum proton energy $E_{p,\max}$ estimated by the TOF detector, we can be confident that within the energy range $[E_{p,\max}/2\ E_{p,\max}]$, only protons are present, with no contribution from other ions.[35] A comparison between the proton spectrum reconstructed by the MFDA and the one obtained from the TPS, positioned at 45° from the target normal and lying in the equatorial plane, is shown in Fig. 9. In the plot, MFDA data are shown using colored symbols within the energy range $[E_{p,\max}/2\ E_{p,\max}]$, where only protons are expected to be present, as previously mentioned. Although the TPS was located close to the MFDA, it was not placed at the same angle or position; therefore, slight differences between the spectra were expected. Nevertheless, the comparison remains meaningful and supports both the reliability of the reconstruction procedure and the good performance of the MFDA. Moreover, in the analysis, we assume that all six diamonds collect identical signals prior to filtering. Although this assumption is reasonable given the small angular spread (~0.9° at PALS), it is still an approximation. Even such limited angles may introduce small variations in the collected signals, depending on the anisotropy of the emitted radiation.

Table I reports the maximum proton energies estimated by both the MFDA and the TPS for shot No. 60 776. The uncertainties result from error propagation associated with the target-to-detector distance. The measured average energies of ~2.25 ± 0.05 MeV (MFDA) and 2.3 ± 0.1 MeV (TPS) show good agreement between the two detectors. The absolute number of protons reconstructed

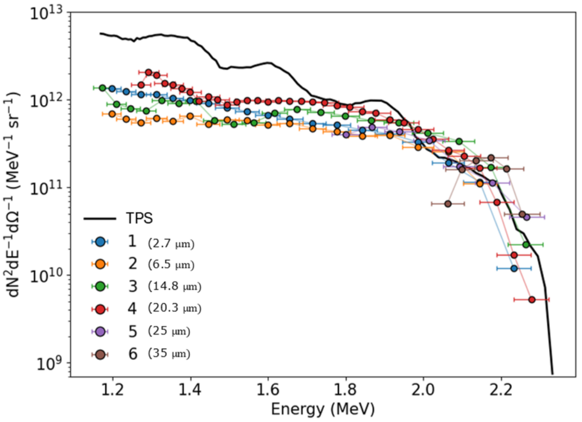

**FIG. 9.** Reconstructed proton spectra: MFDA (colored symbols) and TPS (black line). Uncertainties on the y-axis are ~5% for the MFDA and ~3% for the TPS.

**TABLE I.** Max proton energy detected from MFDA units and comparison of proton yield per steradian with the TPS for shot No. 60 776. TPS detected an $E_{\max}$ = 2.33 MeV.

| Unit | $E_{\max}$ MFDA (MeV) | Protons TPS ($dN/d\Omega$) | Protons MFDA ($dN/d\Omega$) |
|---|---|---|---|
| 1 | 2.23 ± 0.04 | $2.4 \times 10^{12}$ | $4.8 \times 10^{11}$ |
| 2 | 2.20 ± 0.04 | $2.4 \times 10^{12}$ | $3.0 \times 10^{11}$ |
| 3 | 2.26 ± 0.05 | $2.3 \times 10^{12}$ | $3.0 \times 10^{11}$ |
| 4 | 2.27 ± 0.05 | $1.5 \times 10^{12}$ | $2.6 \times 10^{11}$ |
| 5 | 2.27 ± 0.05 | $2.6 \times 10^{11}$ | $6.0 \times 10^{11}$ |
| 6 | 2.25 ± 0.04 | $2.1 \times 10^{10}$ | $1.3 \times 10^{10}$ |

from the TPS and MFDA, within specific energy intervals, is also reported in Table I. These values are obtained by integrating the respective spectra over the energy ranges accessible to each diamond detector, defined by the attenuation characteristics of their corresponding aluminum filters. For consistency, the TPS spectrum was also integrated over the same energy intervals, allowing a direct comparison with each MFDA unit.

In general, the TPS is able to derive the distributions of various populations of particles accelerated from the target and distinguish them by their charge-to-mass ratio.[47] The TPS, however, is not capable of distinguishing alpha particles from the $C^{6+}$ (or from other ion combinations), both having the same charge-to-mass ratio (i.e., 0.5). Placing the MFDA close to the TPS may help resolve this ambiguity, as the resulting signals can be directly compared to validate spectral features. In fact, a given point in the alpha/$C^{6+}$ distribution reconstructed by the TPS would correspond to a specific TOF signal (in both amplitude and timing) that differs significantly depending on whether it originates from an alpha particle or a $C^{6+}$ ion. Indeed, a 4 MeV alpha would overlap (in the time domain) with a $C^{6+}$ only of 12 MeV energy, due to kinematic dependencies ($t \sim E_{kin}/m_i$), and the signal amplitude in diamond will differ depending on whether the detected particle is an alpha or a $C^{6+}$ ion, also accounting for the attenuation introduced by the Al foil placed in front of the detector. Using the SToF code, expected signals were generated from ion distributions measured by the TPS and compared to those experimentally recorded by the MFDA. An example of this comparison is presented in Fig. 10 for shot No. 60 843. In this shot, detectable signals were observed across all six MFDA units. Figure 10(a) presents the proton and alpha/$C^{6+}$ spectra reconstructed from TPS measurements. Figure 10(b) shows the comparison between the MFDA experimental signals (black) and the expected signals (colored) generated using the proton spectrum reconstructed from the TPS. A good qualitative agreement is observed in detectors 3° to 6° in terms of signal shape, amplitude, and modulation, indicating that protons are the dominant contributors to the measured TOF signals under the given conditions. In contrast, detectors 1 and 2 exhibit clear deviations from the expected profiles, consistent with the saturation effect due to high particle flux (decreasing the sensitive area, i.e., with smaller pinholes, should mitigate the saturation). The expected signals in these channels show significantly higher amplitudes than those measured, highlighting a current detection limit of the system under intense flux conditions. In addition, in detector 1, an opposite discrepancy is observed in the time region between 130 and 160 ns, where the measured signal exceeds the synthetic one generated from protons only. This suggests the possible presence of heavier ions contributing to the signal in that time window. Figure 10(c), instead, displays expected signals generated under the assumption that all particles identified by the TPS in the alpha/$C^{6+}$ distribution were alpha particles. These expected signals exhibit amplitudes up to two orders of magnitude lower than the proton-induced signals, suggesting that a possible alpha contribution is negligible in TOF signals in this particular case. Furthermore, the energy spectrum of $C^{6+}$ ions suggests that they would be fully stopped by the aluminum filters used (detectors 3 to 6) or would produce signals of negligibly small amplitude (detectors 1 and 2), excluding any significant contribution from $C^{6+}$ ions to the observed signals.

## F. Comparison with CR-39

When a particle hits the CR-39 plate, it creates a latent track that becomes optically visible after chemical etching. In the present work, the plates were etched in an aqueous solution of 6.25 mol/l NaOH at (70 ± 0.1) °C for the selected etching time. The etching process was then stopped by immersing the detectors in a 2% w/v acetic acid ($CH_3COOH$) solution for 60 min, followed by rinsing in distilled water for 30 min to prevent further chemical action and reduce surface defects. Finally, the plates were dried using an antistatic cloth. Track observation was performed using an optical microscope (Nikon *ECLIPSE Ni-E*). Image acquisition and pit analysis were carried out with the *NIS-Elements BR Analysis* software (version 5.11.00). The analysis consisted of measuring the areas of all visible pits and constructing histograms of the observed track populations. The conversion between pit area and particle energy was performed using previously established calibrations.[48] However, some ambiguity about ions remains due to overlapping pit size–energy relations. This can be partially resolved using prior calibration and foil filters to isolate specific energy ranges and species.[24,48–50]

An additional discrimination analysis method, introduced in this work, consists of directly comparing CR-39 data with TOF measurements by calculating the charge induced in diamond detectors

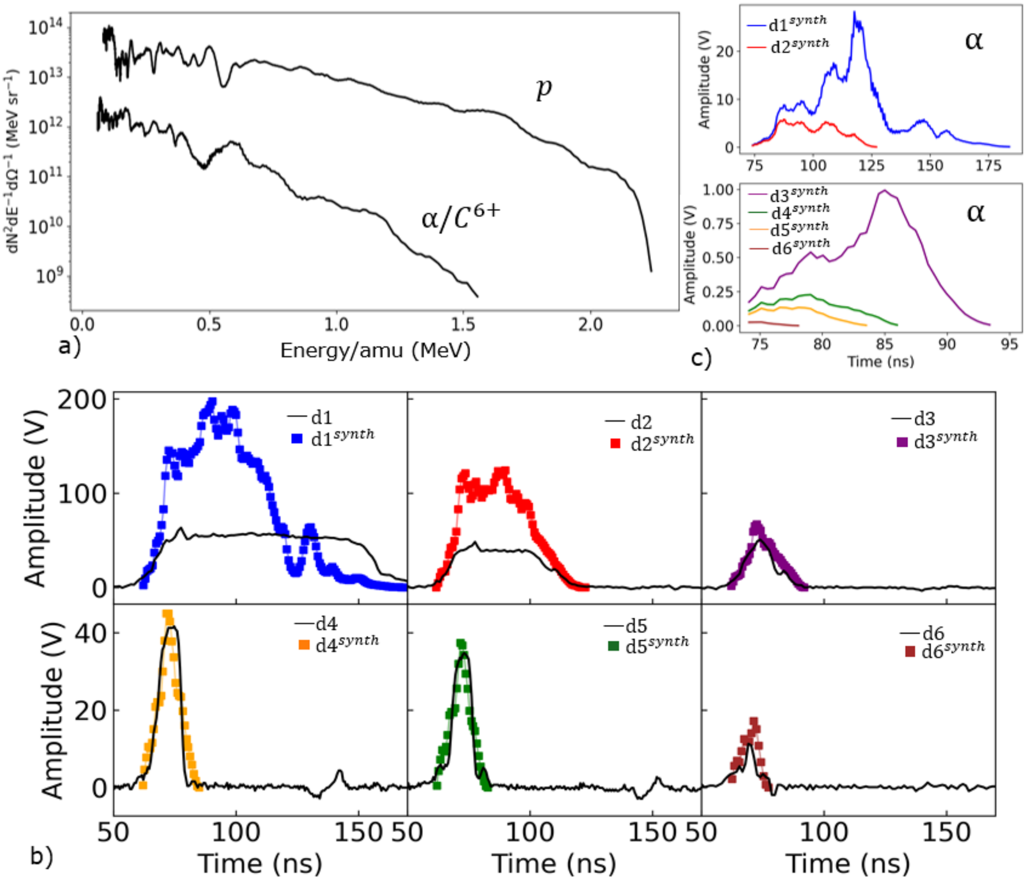

**FIG. 10.** Shot No. 60 843. (a) TPS-reconstructed spectra for protons and the $\alpha$/C$^{6+}$ band. (b) MFDA experimental signals (black) vs synthetic signals (colored) generated from the TPS proton spectrum. (c) Synthetic MFDA signals assuming the entire TPS $\alpha$/C$^{6+}$ band were $\alpha$ particles.

from the particle distributions inferred from CR-39 and correlating it with the experimental MFDA signals. The CR-39 plates were mounted inside the MFDA vacuum flange and equipped with aluminum filters of the same thickness as those used in front of the diamond detectors. These filters selectively attenuate low-energy particles, thus defining a well-defined energy window for the detected pit population. For each energy bin $i$ of the reconstructed CR-39 histogram, characterized by a population $N_i$ and a central energy value $\bar{E}_i$, an expected synthetic induced charge $\bar{Q}_i^{\text{syn}}$ in diamond can be calculated according to Eq. (1), taking into account the energy losses in the corresponding filters. Each central energy value, $\bar{E}_i$, is then mapped to a specific time-of-flight through Eq. (2), and the bin edges define a corresponding time interval in the TOF domain. The experimental MFDA signal is integrated over this time interval, yielding a quantity directly comparable with the synthetic charge derived from the CR-39 data. To ensure a meaningful comparison, the resulting time-bin width is chosen to be no smaller than the temporal resolution of the acquisition system.

An example of this comparison is provided by the results from shot No. 60 866, as shown in Fig. 11. Starting from the energy histograms obtained from the CR-39 detector for two species (protons and alpha particles) derived from the same pit population [Fig. 11(a)], the induced charges in diamond were calculated and compared with MFDA measurements. Three sets of comparisons are reported, corresponding to three diamond detectors equipped with aluminum filters of 2.7, 6.5, and 14.8 $\mu$m thickness. The results are plotted in Fig. 11(b). In each case, calculated charge values are plotted as a function of energy: red points represent the charge assuming the pits originate from alpha particles, while blue points assume the same pit distribution originates from protons. Both reconstructions are based on the same CR-39 detector. Although qualitative and based on several assumptions, the results show that the proton-based reconstruction is in better agreement with the experimental signals obtained from the MFDA. This method was applied here specifically for protons and alpha particles, for which calibration data were available. The same approach can be extended to any ion pair for which

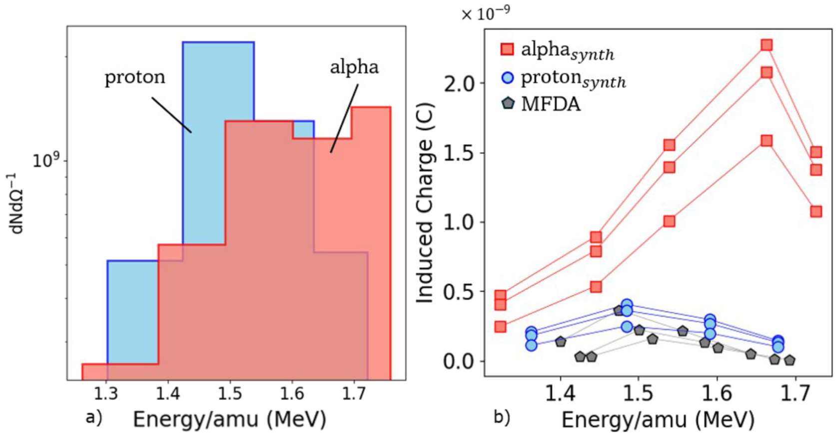

**FIG. 11.** (a) Proton (blue) and alpha particle (red) energy histograms obtained with the CR-39 analysis considering the same pit populations. (b) Synthetic induced charge values for alpha particles (red) and protons (blue) obtained with CR-39 compared with experimental data (gray) from MFDA for shot No. 60 866.

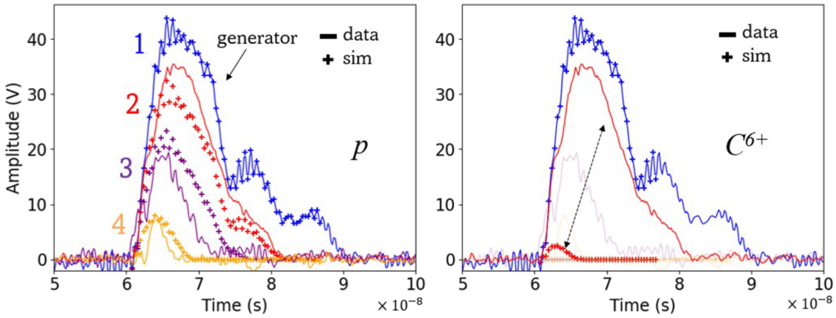

**FIG. 12.** Signals from four MFDA units (line) compared with corresponding simulated signals (cross) using signal 1 as the generator for protons (left) and carbons (right) for shot No. 60 777.

discrimination is challenging, such as alpha particles and carbon ions and beyond.

### G. Self-cross check

The MFDA also allows for a real-time and self-checking procedure based on expected signal modeling. In this approach, a particle spectrum (i.e., for protons or carbons) is inferred from one detector signal, referred to as the "generator," and used to simulate the expected responses of the other MFDA units, considering their respective aluminum filters and under the assumption that all detectors receive the same incident particle distribution. If the assumed ion species is correct, the simulated signals will match the experimental ones. This enables a fast verification of particle identification assumptions, as illustrated in Fig. 12 for shot No. 60 777. The left panel shows the comparison for protons (good match); the right panel shows the same for $C^{6+}$ ions (poor match), validating the method's feasibility. The method can be selectively applied to portions of the signal where dominance of a particular species is suspected. This approach could also help validate or extend confidence intervals in the reconstructed spectra, potentially allowing more accurate proton spectrum extrapolations beyond conventional TOF limits.

## IV. CONCLUSION

A Multi Filter Diamond Array (MFDA), composed of six thin CVD diamond detectors in a sandwich configuration, equipped with six different aluminum filters, was developed at the University of Rome "Tor Vergata" laboratories for ion discrimination in laser-driven fusion experiments. The detector was tested as a time-of-flight particle detector at the PALS facility in Prague, within the framework of the INFN FUSION project. The results were successfully compared and validated against a TPS placed nearby in the interaction chamber. Furthermore, MFDA effectiveness for real-time measurement of the x-ray mean energy emitted from the laser-target interaction in a single shot was shown. Two cross-check methods with other diagnostics, such as the TPS and CR-39, based on the induced signal shape and amplitude in the MFDA units, are presented, enabling also investigation of potential detector saturation effects that can be mitigated by reducing the sensitive area with smaller pinholes. In addition, the aluminum filters employed in this campaign were rather aggressive for heavier ions, making the MFDA response largely proton-dominated. In future campaigns, the use of modular filter assemblies with finer thickness steps is planned to better tailor the detection range to the observed ion energies.

The MFDA allows for a real-time internal self-checking procedure: by using one detector signal to generate expected responses across the array, it is possible to verify particle identity assumptions and assess the consistency of the measured data. This method can also help refine confidence intervals in the reconstructed spectra and may enable more accurate spectrum extrapolation beyond standard TOF limits. A forward-fitting approach, in which simulated TOF signals are iteratively matched to experimental data to infer ion distributions, represents a promising direction for enhancing the

MFDA's species and energy discrimination capabilities. Although not implemented in this work due to limited data availability, this methodology may support future developments, including potential real-time applications. This developed device will be further used in the next laser–plasma experiments to enable additional improvements and developments. Overall, this work also aims to pave the way for future studies that combine online and offline synthetic signal analysis of TOF methods with complementary diagnostics, thereby broadening the scope and accuracy of ion characterization in laser–plasma experiments.

## ACKNOWLEDGMENTS

The authors wish to thank LASERLAB for the support given for the experiment "FUSION: Maximizing the p(11B, $\alpha$)2$\alpha$ reaction using in-plasma and pitcher target configurations and novel target design" (PID No. 26286). This work has also been carried out within the framework of the COST Action CA21128-PROBONO "PROton BOron Nuclear fusion: from energy production to medical applications," supported by COST (European Cooperation in Science and Technology—www.cost.eu).

## AUTHOR DECLARATIONS

### Conflict of Interest

The authors have no conflicts to disclose.

### Author Contributions

**Angelo M. Raso**: Conceptualization (lead); Data curation (lead); Formal analysis (lead); Investigation (lead); Methodology (lead); Software (lead); Validation (lead); Writing – original draft (lead); Writing – review & editing (lead). **Edoardo Domenicone**: Data curation (equal). **Giada Petringa**: Data curation (equal). **Fabrizio Consoli**: Supervision (equal); Visualization (equal); Writing – review & editing (equal). **Farmesk Abubaker**: Data curation (equal); Supervision (equal); Writing – review & editing (equal). **Massimiliano Scisciò**: Data curation (equal); Supervision (equal); Visualization (equal); Writing – review & editing (equal). **G. A. Pablo Cirrone**: Supervision (equal); Writing – review & editing (equal). **Shubham Agarwal**: Data curation (supporting). **Massimo Alonzo**: Data curation (supporting). **Carmen Altana**: Data curation (supporting). **Sahar Arjmand**: Data curation (supporting). **Caterina Ciampi**: Visualization (supporting). **Mattia Cipriani**: Data curation (supporting); Visualization (supporting). **Pooja Devi**: Visualization (supporting). **Francesco Filippi**: Visualization (supporting). **Pavel Gajdos**: Data curation (supporting); Visualization (supporting). **Benoist Grau**: Data curation (supporting); Visualization (supporting). **Giovanni Luca Guardo**: Data curation (supporting); Visualization (supporting). **Josef Krasa**: Data curation (supporting); Visualization (supporting). **Michal Krupka**: Data curation (supporting); Visualization (supporting). **Salvatore Mirabella**: Visualization (supporting). **Giovanni Morello**: Data curation (supporting); Visualization (supporting). **Massimo Nocente**: Data curation (supporting); Visualization (supporting). **Fabrizio Odorici**: Data curation (supporting); Visualization (supporting). **Gabriele Pasquali**: Data curation (supporting); Visualization (supporting). **Antonino Picciotto**: Data curation (supporting); Visualization (supporting). **Rosaria Rinaldi**: Data curation (supporting); Visualization (supporting). **Marcin Rosinski**: Data curation (supporting); Visualization (supporting). **Antonino Scandurra**: Data curation (supporting); Visualization (supporting). **Sushil Singh**: Data curation (supporting); Visualization (supporting). **Przemyslaw Tchorz**: Data curation (supporting); Visualization (supporting). **Gianluca Verona Rinati**: Visualization (supporting). **Claudio Verona**: Conceptualization (equal); Data curation (equal); Formal analysis (equal); Investigation (equal); Methodology (equal); Supervision (equal); Validation (equal); Visualization (equal); Writing – original draft (equal); Writing – review & editing (equal).

## DATA AVAILABILITY

The experimental data used to support the findings of this study are available from the corresponding author upon reasonable request.

## REFERENCES

[1] H. Daido, M. Nishiuchi, and A. S. Pirozhkov, Rep. Prog. Phys. **75**, 056401 (2012).

[2] A. Macchi, *A Superintense Laser-Plasma Interaction Theory Primer* (Springer, Heidelberg, 2013).

[3] D. Doria, K. F. Kakolee, S. Kar, S. K. Litt, F. Fiorini, H. Ahmed, S. Green, J. C. G. Jeynes, J. Kavanagh, D. Kirby *et al.*, AIP Adv. **2**, 011209 (2012).

[4] P. Chaudhary, G. Milluzzo, H. Ahmed, B. Odlozilik, A. McMurray, K. M. Prise, and M. Borghesi, Front. Phys. **9**, 624963 (2021).

[5] M. Barberio, S. Veltri, M. Scisciò, and P. Antici, Sci. Rep. **7**, 40415 (2017).

[6] S. Atzeni and J. M. ter Vehn, *The Physics of Inertial Fusion: Beam Plasma Interaction, Hydrodynamics, Hot Dense Matter* (Oxford University Press, Oxford, 2004).

[7] A. J. Donné, J. Fusion Energy **38**, 503 (2019).

[8] M. L. E. Oliphant and E. Rutherford, Proc. R. Soc. London, Ser. A **141**, 259 (1933).

[9] C. Labaune, C. Baccou, V. Yahia, C. Neuville, and J. Rafelski, Sci. Rep. **6**, 21202 (2016).

[10] H. W. Becker, C. Rolfs, and H. P. Trautvetter, Z. Phys. A **327**, 341 (1987).

[11] *Laser–Plasma Interactions and Applications*, *Scottish Graduate Series*, edited by P. McKenna, D. Neely, R. Bingham, and D. A. Jaroszynski (Springer International Publishing, Heidelberg, 2013).

[12] M. Salvadori, G. D. Giorgio, M. Cipriani, M. Scisciò, C. Verona, P. L. Andreoli, G. Cristofari, R. D. Angelis, M. Pillon, N. E. Andreev *et al.*, High Power Laser Sci. Eng. **10**, e6 (2022).

[13] M. Cutroneo, P. Musumeci, M. Zimbone, L. Torrisi, F. La Via, D. Margarone, A. Velyhan, J. Ullschmied, and L. Calcagno, J. Mater. Res. **28**, 87 (2013).

[14] M. Marinelli, E. Milani, G. Prestopino, C. Verona, G. Verona-Rinati, M. Cutroneo, L. Torrisi, D. Margarone, A. Velyhan, J. Krasa, and E. Krousky, Appl. Surf. Sci. **272**, 104 (2013).

[15] A. Yogo, H. Daido, A. Fukumi, Z. Li, K. Ogura, A. Sagisaka, A. S. Pirozhkov, S. Nakamura, Y. Iwashita, T. Shirai *et al.*, Phys. Plasmas **14**, 043104 (2007).

[16] P. Bellido, R. Lera, M. Seimetz, A. R.-d. l. Cruz, S. Torres-Peirò, M. Galán, P. Mur, I. Sánchez, R. Zaffino, L. Vidal *et al.*, J. Instrum. **12**, T05001 (2017).

[17] V. Scuderi, G. Milluzzo, D. Doria, A. Alejo, A. G. Amico, N. Booth, G. Cuttone, J. S. Green, S. Kar, G. Korn *et al.*, Proc. R. Soc. London, Ser. A **978**, 164364 (2020).

[18] M. Reimold, S. Assenbaum, C. Bernert, E. Beyreuther, F.-E. Brack, L. Karsch, S. D. Kraft, F. Kroll, M. Loeser, A. Nossula *et al.*, Sci. Rep. **12**, 21488 (2022).

[19] *CVD Diamond for Electronic Devices and Sensors*, edited by R. S. Sussmann (John Wiley & Sons, Chichester, 2009).

[20] *Diamond: Electronic Properties and Applications*, edited by L. S. Pan and D. R. Kania (Springer, New York, 1995).

[21] M. S. Schollmeier, J. J. Bekx, J. Hartmann, E. Schork, M. Speicher, A. F. Brodersen, A. Fazzini, P. Fischer, E. Gaul, B. Gonzalez-Izquierdo *et al.*, Sci. Rep. **13**, 18155 (2023).

[22] M. Seimetz, J. Peñas, J. J. Llerena, J. Benlliure, J. García-López, M. Millán-Callado, and J. M. Benlloch, Phys. Med. **76**, 72 (2020).

[23] Y. Zhang, H.-W. Wang, Y.-G. Ma, L.-X. Liu, X.-G. Cao, G.-T. Fan, G.-Q. Zhang, and D.-Q. Fang, Nucl. Sci. Tech. **30**, 87 (2019).

[24] T. W. Jeong, P. K. Singh, C. Scullion, H. Ahmed, P. Hadjisolomou, C. Jeon, H. Yun, K. F. Kakolee, M. Borghesi, and S. Ter-Avetisyan, Sci. Rep. **7**, 2152 (2017).

[25] J. J. Thomson, Proc. R. Soc. London, Ser. A **89**, 1 (1913).

[26] C. Baccou, V. Yahia, S. Depierreux, C. Neuville, C. Goyon, F. Consoli, R. De Angelis, J. E. Ducret, G. Boutoux, J. Rafelski, and C. Labaune, Rev. Sci. Instrum. **86**, 083307 (2015).

[27] F. Consoli, M. Cipriani, M. Salvadori, G. Cristofari, P. L. Andreoli, N. D'Olivio, G. Milluzzo, L. Torrisi, D. Margarone, G. Korn *et al.*, J. Instrum. **11**, C05010 (2016).

[28] V. Kantarelou, A. Velyhan, P. Tchórz, M. Rosinski, G. Petringa, G. A. P. Cirrone, V. Istokskaia, J. Krása, M. Krůs, A. Picciotto *et al.*, Laser Part. Beams **2023**, e10 (2023).

[29] C. Verona, M. Marinelli, A. M. Raso, G. Verona Rinati, G. A. P. Cirrone, G. Petringa, L. Giuffrida, J. Dostál, M. Krupka, F. Consoli *et al.*, J. Instrum. **18**, C07008 (2023).

[30] P. Gibbon, *Short Pulse Laser Interactions with Matter: An Introduction* (Imperial College Press, London, 2005).

[31] Almax easyLab, Official website, https://www.almax-easylab.com/ (accessed September 2025).

[32] M. Angelone and C. Verona, J. Nucl. Eng. **2**, 422 (2021).

[33] J. F. Ziegler, Nucl. Instrum. Methods Phys. Res., Sect. B **219–220**, 1027–1036 (2004).

[34] G. Milluzzo, V. Scuderi, A. Alejo, A. G. Amico, N. Booth, M. Borghesi, G. A. P. Cirrone, G. Cuttone, D. Doria, J. Green *et al.*, Rev. Sci. Instrum. **90**, 083303 (2019).

[35] M. Salvadori, F. Consoli, C. Verona, M. Cipriani, M. P. Anania, P. L. Andreoli, P. Antici, F. Bisesto, G. Costa, G. Cristofari *et al.*, Sci. Rep. **11**, 3071 (2021).

[36] C. Cercignani, in *Rarefied Gas Dynamics*, edited by S. S. Fisher (AIAA, New York, 1981), Vol. 1, p. 305.

[37] A. Miotello and R. Kelly, Appl. Surf. Sci. **138–139**, 44–51 (1999).

[38] M. R. D. Rodrigues, A. Bonasera, M. Scisciò, J. A. Pérez-Hernández, M. Ehret, F. Filippi, P. L. Andreoli, M. Huault, H. Larreur, D. Singappuli *et al.*, Matter Radiat. Extremes **9**, 037203 (2024).

[39] P. Mora, Phys. Rev. Lett. **90**, 185002 (2003).

[40] S. Stave, M. W. Ahmed, R. H. France III, S. S. Henshaw, B. Müller, B. A. Perdue, R. M. Prior, M. C. Spraker, and H. R. Weller, Phys. Lett. B **696**, 26–31 (2011).

[41] J. Allison, K. Amako, J. Apostolakis, P. Arce, M. Asai, T. Aso, E. Bagli, A. Bagulya, S. Banerjee, G. Barrand *et al.*, Nucl. Instrum. Methods Phys. Res., Sect. A **835**, 186–225 (2016).

[42] J. Allison, K. Amako, J. Apostolakis, H. Araujo, P. Arce Dubois, M. Asai, G. Barrand, R. Capra, S. Chauvie, R. Chytracek *et al.*, IEEE Trans. Nucl. Sci. **53**, 270 (2006).

[43] S. Agostinelli, J. Allison, K. Amako, J. Apostolakis, H. Araujo, P. Arce, M. Asai, D. Axen, S. Banerjee, G. Barrand *et al.*, Nucl. Instrum. Methods Phys. Res., Sect. A **506**, 250 (2003).

[44] F. Consoli, V. T. Tikhonchuk, M. Bardon, P. Bradford, D. C. Carroll, J. Cikhardt, M. Cipriani, R. J. Clarke, T. E. Cowan, C. N. Danson *et al.*, High Power Laser Sci. Eng. **8**, e22 (2020).

[45] D. Margarone, L. Torrisi, S. Cavallaro, E. Milani, G. Verona-Rinati, M. Marinelli, C. Tuvè, L. Láska, J. Krása, M. Pfeifer *et al.*, Radiat. Eff. Defects Solids **163**, 463 (2008).

[46] National Institute of Standards and Technology (NIST), X-ray mass attenuation coefficients—Aluminum (z = 13), https://physics.nist.gov/PhysRefData/XrayMassCoef/ElemTab/z13.html (accessed September 2025).

[47] M. Scisciò, G. D. Giorgio, P. L. Andreoli, M. Cipriani, G. Cristofari, R. D. Angelis, M. Salvadori, G. A. P. Cirrone, L. Giuffrida, D. Margarone *et al.*, Laser Part. Beams **2023**, e14.

[48] G. Petringa, V. Kantarelou, R. Catalano, G. Cantone, O. Giampiccolo, G. E. Messina, G. Angemi, S. Arjmand, E. Caruso, G. Cuttone *et al.*, J. Instrum. **19**, C04044 (2024).

[49] M. Seimetz, P. Bellido, P. García, P. Mur, A. Iborra, A. Soriano, T. Hülber, J. G. López, M. C. Jiménez-Ramos, R. Lera, A. R. de la Cruz, I. Sánchez, R. Zaffino, L. Roso, and J. M. Benlloch, Rev. Sci. Instrum. **89**, 023302 (2018).

[50] M. Huault, T. Carrière, H. Larreur, P. Nicolaï, D. Raffestin, D. Singappuli, E. D'Humières, D. Dubresson, K. Batani, M. Cipriani *et al.*, Phys. Plasmas **32**, 013102 (2025).